Finite Element Analysis to Investigate Variability of MR Elastography in the Human Thigh

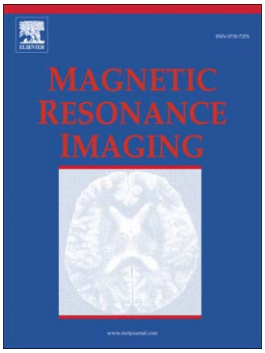

Finite Element Analysis to Investigate Variability of MR Elastography in the Human Thigh

L. Hollis, E. Barnhill, M. Perrins, P. Kennedy, N. Conlisk, C. Brown, P.R. Hoskins, P. Pankaj, N. Roberts

PII: S0730-725X(17)30112-1
DOI: doi:10.1016/j.mri.2017.06.008
Reference: MRI 8780

To appear in: *Magnetic Resonance Imaging*

Received date: 12 July 2016
Revised date: 14 May 2017
Accepted date: 16 June 2017

Please cite this article as: Hollis L, Barnhill E, Perrins M, Kennedy P, Conlisk N, Brown C, Hoskins PR, Pankaj P, Roberts N, Finite Element Analysis to Investigate Variability of MR Elastography in the Human Thigh, *Magnetic Resonance Imaging* (2017), doi:10.1016/j.mri.2017.06.008

Finite Element Analysis to Investigate Variability of MR Elastography in the Human Thigh

L. Hollis[a,*], E. Barnhill[b], M. Perrins[a], P. Kennedy[c], N. Conlisk[d], C. Brown[e], P.R. Hoskins[d], P. Pankaj[f], N .Roberts[a,**]

[a] *University of Edinburgh, Clinical Research Imaging Centre, 47 Little France Crescent, Edinburgh, EH16 4TJ, United Kingdom*
[b] *Charité Universitatsmedizin Berlin, Charitéplatz 1, 10117, Berlin, Germany*
[c] *Icahn School of Medicine, Mount Sinai, 1 Gustave L. Levy Place, New York, United States of America*
[d] *University of Edinburgh, Centre for Cardiovascular Sciences, 47 Little France Crescent, Edinburgh, EH16 4TJ, United Kingdom*
[e] *Research and Development, The Mentholatum Company, East Kilbride, G74 5PE, United Kingdom*
[f] *School of Engineering, University of Edinburgh, King's Buildings, Mayfield Road, Edinburgh, EH9 3JL, United Kingdom*

Abstract

Purpose: To develop finite element analysis (FEA) of magnetic resonance elastography (MRE) in the human thigh and investigate inter-individual variability of measurement of muscle mechanical properties.
Methods: Segmentation was performed on MRI datasets of the human thigh from 5 individuals and FEA models consisting of 12 muscles and surrounding tissue created. The same material properties were applied to each tissue type and a previously developed transient FEA method of simulating MRE using *Abaqus* was performed at 4 frequencies. Synthetic noise was applied to the simulated data at various levels before inversion was performed using the Elastography Software Pipeline. Maps of material properties were created and visually assessed to determine key features. The coefficient of variation (CoV) was used to assess the variability of measurements in each individual muscle and in the groups of muscles across the subjects. Mean

*Corresponding author
**Principal corresponding author
Email address: lyamhollis@outlook.com (L. Hollis)

measurements for the set of muscles were ranked in size order and compared with the expected ranking.
Results: At noise levels of 2% the CoV in measurements of $|G^*|$ ranged from 5.3 to 21.9% and from 7.1 to 36.1% for measurements of ϕ in the individual muscles. A positive correlation (R^2 value 0.80) was attained when the expected and measured $|G^*|$ ranking were compared, whilst a negative correlation (R^2 value 0.43) was found for ϕ.
Conclusions: Created elastograms demonstrated good definition of muscle structure and were robust to noise. Variability of measurements across the 5 subjects was dramatically lower for $|G^*|$ than it was for ϕ. This large variability in ϕ measurements was attributed to artefacts.

Keywords: finite element analysis, magnetic resonance elastography, elastography software pipeline, human thigh

1. Introduction

Material properties of the human leg vary through natural physiological processes, such as muscle contraction [1] and aging [2], and through disease states, such as myofascial pain syndrome [3]. A non-invasive method of measuring such properties *in vivo* is magnetic resonance elastography (MRE). MRE utilises a phase-encoding gradient to visualise displacements resulting from mechanically induced shear waves in order to probe the material properties of *in vivo* tissue [4, 5]. Typically a map of these material properties, known as an elastogram, is created using an inversion algorithm [6, 7]. A recent development in the field has been the creation and implementation of the multi-frequency dual elasto-visco (MDEV) inversion algorithm [8], which combines displacements from multiple frequencies in order to reduce frequency dependent artefacts [9, 10, 11, 12].

A recent study by this group [13] demonstrated that whilst MDEV achieved an improvement in the quality of the elastogram in comparison to direct inversion at a single frequency (DI), measurements through both algorithms were dependent upon the geometry of the structure under investigation as well as the material properties. Whilst this study utilised idealised geometries, there are potential practical implications given the often large inter-individual variability in the size and shape of anatomical structures. Indeed, this is true of the human leg, where muscle structure can vary significantly from one individual to another and is dependent on multiple factors such as

age, sex, height and exercise habits of the individual [14].

An increasingly common method of experimentation in the MRE field is finite element analysis (FEA). Using FEA, datasets are created *in silico* that can then be integrated into MRE post-processing software. The specific benefit of FEA over *in vivo* or phantom studies is the level of control that the researcher has over aspects such as the geometry and material properties of the model, and noise levels in the resulting synthetic datasets. Traditionally, such studies have utilised simplistic geometries to validate or test the limitations of inversion algorithms [15, 16, 17, 18, 12]. More recently, however, focus has turned to anatomical structures. Of note in this regard, Thomas-Seale et. al (2016) [19] used FEA to investigate arterial stenosis, demonstrating the ability of the technique to differentiate between lipid and fibrotic plaques. Meanwhile a study by McGrath et al. (2015) [20] simulated 3-D wave propagation in the human brain, raising concerns over whether MRE would be able to detect the subtle change in stiffness through dementia over the errors in MRE measurements resulting from interference patterns and heterogeneity of human tissue.

The present study aims to develop and utilise FEA models to assess the variability of MDEV measurements from the muscles of the human thigh in a cohort of healthy volunteers.

2. Methods

2.1. Overview

MRI datasets were acquired for 5 healthy male volunteers aged 20-32 (mean of 25). Segmentation was then performed upon these images and FE models created. Material properties were defined consistently for each muscle across the set of models. Once the simulation had run, the displacements resulting from the induced wave propagation were extracted and exported to post-processing software, where the inversion was performed using the Elastography Software Pipeline (ESP) [12]. The variability in measurements across the different set of models was then assessed.

2.2. MRI Acquisition

MRI was performed on a 3 T scanner (*Verio, Siemens, Erlangen, Germany*) using a single-shot spin-echo sequence with FoV of 200 x 200 mm^3 and 48 slices corresponding to a voxel size of 0.39 x 0.39 x 3.3 mm^3.

2.3. Image Segmentation

Manual segmentation was performed on each set of images using *Scan IP (Simpleware, Exeter, UK)*. Masks were created for twelve different muscles, the femoral bone and all other tissue, termed from here on as the surrounding tissue (figure 1). To allow for better smoothing, the masks were re-sampled in the z-direction by linearly interpolating to a pixel spacing of 1 mm. For the purposes of efficiency with regards to the modelling, the masks were cropped such that only the upper 10 cm of the scans were included in the model.

2.4. Finite Element Analysis

An explicit transient methodology for simulating MRE as previously described in [13, 21] was utilised in *Abaqus/explicit (Dassault Systéme, Simulia Corp., Providence, Rhode Island, USA)*. In this approach, the load is applied throughout the entire time that the simulation is run. Displacement are output at 8 time-points evenly spaced across a single wave cycle at the frequency of interest. For the present study, the simulation was allowed to run for 0.052 s before outputting data in order to allow the wave to propagate throughout the entire model.

2.4.1. Mesh

Meshing was performed in *Scan IP* with minimum and maximum edge lengths of 1 and 1.25 mm respectively using linear tetrahedral elements (C3D4). Table 1 summarises the number of elements in each model.

Boundary and loading Conditions

The peripheral surfaces of the model in the z-direction were fixed with no translation or rotation permitted. In order to reduce simulation time, the bone was removed from the model and the ensuing surface, representing the boundary between the bone and other tissues, also fixed. During the meshing procedure the muscles and surrounding tissue were merged together to form a single part. This has previously been shown to have the same effect as applying tie constraints between the different regions [21].

The load was applied via a concentrated force in the z-direction acting on a ring of nodes on the surface of the leg in the central 5 cm of the model (figure 2). This was seen as representative of the circular ring actuator that is often used for inducing vibrations into the leg [22, 1]. Frequencies of 25, 37.5, 50 and 62.5 Hz were applied [22, 12]. Based upon comparisons of the amplitudes of the wave in the models and *in vivo* scans, the total force applied over all the elements in the model was 10 N (table 1).

Convergence Studies

Convergence studies were performed based on the criteria outlined in [21]. Meshes were defined with minimum edge lengths of 1, 1.5, 2, 2.5 and 3 mm. The load was applied through the same area on the surface of each model, with the force per node adjusted so that the total load applied remained consistent in each case. Convergence was assumed to have been achieved when the change in mean $|G^*|$ and ϕ values from one refinement to the next was less than 2% in all of the regions of interest in the model.

2.4.2. Material Properties

There has been relatively little previous work undertaken to measure the material properties of all muscles in the leg simultaneously in the frequency range of interest in the present study. A previous MRE study by Chakouch et al. (2015) [23] demonstrated that of four rheological models tested, the Zener model of viscoelasticity provided the best fit to muscles in the upper leg and this model was used to define material properties here. The model consists of a spring, μ_1, connected in parallel with a series connection of a dashpot, η, and spring, μ_2 (see figure 3). The resulting equation that governs the shear modulus in the Zener model is:

$$G_M(\omega) = \frac{\mu_1\mu_2 + i\omega\eta\,(\mu_1 + \mu_2)}{\mu_2 + i\omega\eta} \tag{1}$$

where ω represents the angular frequency of the propagating shear wave.

The model parameters for the biceps, gracilis, semitendinosus and semimembranosus muscles were calculated in the aforementioned Chakouch study and have been utilised here. Klatt et al. (2010) [22] calculated storage and loss modulus values at multiple frequencies for the grouped quadricep muscles (rectus femoris, vastus medialis, vastus intermedius and vastus lateralis). Parameters for the Zener model based on these measurements were calculated by minimising the cost function in the same manner as previous studies [24, 23]:

$$\chi = \sum_{n=1}^{N} \sqrt{(\Re\left[G(\omega_n) - G_M(\omega_n)\right])^2 + (\Im\left[G(\omega_n) - G_M(\omega_n)\right])^2} \tag{2}$$

where $G_M(\omega)$ represents the complex shear modulus for the Zener model iterated over, $G(\omega)$ represents the complex shear modulus as measured using MRE, and N represents the number of frequencies used.

Whilst the calculated viscous values was similar to those from the Chakouch study (and therefore used here), the elastic parameters were 4-5 times smaller. Based on observations from *in house* elastograms, it was determined that such variation was unrealistic. As such, the mean μ_1 and μ_2 values were calculated for the muscles from Chakouch study, and the elastic components were normalised using the mean of the elastic measurements of the same muscles made by a separate Chakouch et al. (2015) [25] study, which investigated the elastic properties of 11 muscles in the thigh.

The remaining tissues without definition were the sartorius and adductor muscles, and the surrounding tissue. There are no published values of the mechanical properties of these muscles at multiple frequencies. The elastic properties of the sartorious muscle and surrounding tissue were measured in the study by Chakouch et al. (2015) [25], and therefore the same normalisation process described previously was used to calculate the elastic components with which to define this muscle. The mean values of the components for all of the other muscles were used to define the viscous components of the adductor and sartorius muscles and the surrounding tissue, and the elastic components of the adductor muscles. The components used for all tissue types are summarised in table 2.

2.4.3. Data Processing

Nodal coordinates and corresponding displacements in each spatial direction and at each time-point were extracted from the *.odb* file created by *Abaqus* during simulation and written to *.txt* files. These were then imported into *Matlab* where displacements were interpolated to a newly created, evenly spaced grid. Spacing between neighbouring points was 2 mm in all directions thus representing an MRE scan with a 2 x 2 x 2 mm^3 voxel size, and the grid was centered on the central axial plane of the model. The size of the grid varied in the x and y-axial planes depending on the size of the leg, but was spread over 40 mm in the z-direction.

Gaussian noise [26] was added to the wave images based on the method outlined by Miller et al. (2015) [27]. Noise levels were varied from 0 to 10%.

2.5. Inversion and Post-Processing

Inversion was performed using the Elastography Software Pipeline (ESP) [12]. The basis for inversion in ESP are the MDEV equations [8]:

$$|G^*| = \rho \frac{\sum_{m=1}^{3} \sum_{n=1}^{N} \omega_n^2 \left| u_m^* \left(\omega_n \right) \right|}{\sum_{m=1}^{3} \sum_{n=1}^{N} \nabla^2 \left| u_m^* \left(\omega_n \right) \right|} \tag{3}$$

$$\phi = \cos^{-1}\left(-\frac{\sum_{m=1}^{3}\sum_{n=1}^{N}\left[\Delta u'_m(\omega_n)\,u'_m(\omega_n) + \Delta u''_m(\omega_n)\,u''_m(\omega_n)\right]}{\sum_{m=1}^{3}\sum_{n=1}^{N}\left|\Delta u^*_m(\omega_n)\right|\left|u^*_m(\omega_n)\right|}\right) \quad (4)$$

Here u' and u'' represent the real and imaginary components of the displacement, u^*, whilst $|G^*|$ and ϕ represent quantities akin to the traditional magnitude and phase of the complex shear modulus, but with contributions averaged over multiple frequencies. ESP also employs wavelet-domain denoising techniques to remove both low and high frequency noise contributions.

Masks representing the region of interest (ROI) for each muscle were created and applied to the elastograms in order to calculate the mean values of $|G^*|$ and ϕ in each muscle. To achieve this, the set of elements that constituted each material were identified from the *Abaqus .inp* file and matched to the nodes from which they were constructed. A value of one was assigned to those elements within the material element set, whilst a value of zero was assigned for all nodes outside the element set. These values could then be interpolated to the same coordinate grid as used for importing the wave images thus creating a mask for each individual muscle.

In order to assess the effectiveness of the algorithm in terms of its ability to map the material properties, the prescribed and measured $|G^*|$ and ϕ values were ranked in order of highest to lowest value and these rankings compared to one another. Additionally, combined measurements of $|G^*|$ and ϕ were made in the quadriceps, hamstring and medial muscle groups. The ratio of the values the measurements made from one group to another was then calculated and compared with the expected ratio.

To investigate the variability in measurements across the volunteer cohort, the coefficient of variation was calculated as a percentage:

$$c_v = 100 \cdot \frac{\sigma}{\mu} \quad (5)$$

where μ is equal to the mean of the measurements from the 5 volunteers and σ represents the standard deviation of the acquired measurements. The coefficient of variation was calculated for each muscle individually and for the three muscle groups.

To assess the influence of size upon the variability of measurements, the coefficient of variation for each muscle was plotted against the mean size of the ROI for that muscle across the 5 patients, linear regression performed and the coefficient of determination (R^2 value) calculated.

3. Results

Examples of the complex displacement images and $|G^*|$ and ϕ elastograms for each leg are presented in figure 4. Definition of the different muscles and variation in their measurements could be clearly seen for many of the muscles in the $|G^*|$ elastograms. Artefacts often dominated the boundaries between materials in the ϕ elastograms. The application of noise to the displacement data tended to result in a slight decrease in measurements of $|G^*|$, but a slight increase in measurements of ϕ. In both instances, the definition of the boundaries between muscles in the elastogram became less clear with increasing noise (figure 5).

Measurements of $|G^*|$ and ϕ in the individual muscles have been compared to the expected values in figure 6 a-b. Whilst measurements of $|G^*|$ tend to be relatively accurate, this is not the case for ϕ where measurements are typically overestimated. The ranking in $|G^*|$ and ϕ of the expected measurement has been compared against the ranking of actual measurement in figure 6 c-d. For $|G^*|$ there was a clear positive relationship between the measured and expected rank (R^2 value 0.80). For ϕ the relationship represented a negative trend (R^2 value of 0.43).

The coefficient of variation was dependent upon the muscle under investigation. At a noise level of 2% the coefficient of variation in the measurements of $|G^*|$ ranged from 5.29 to 21.90%, with these values occurring in the biceps femoris short head and sartorius muscles respectively. For ϕ values were typically higher with a range from was 7.07 (vastus intermedius) to 36.08% (rectus femoris) (table 3). There appeared to be no direct relationship between the coefficients of variability for $|G^*|$ and ϕ. For $|G^*|$ the coefficient of variation tended to increase with increasing noise, whilst the opposite was true for ϕ (figure 7). There was no clear linear relationship between the coefficient of variation calculated for $|G^*|$ or ϕ across each muscle in the 5 legs and the mean size of the region of interest for that muscle with R^2 values less than 0.1 figure 6 d-e).

With regards to the muscle groups, the coefficient of variation was lowest in the medial muscles for both $|G^*|$ and ϕ. For $|G^*|$ the coefficient of variation for the group as a whole was slightly lower than the mean of the coefficient of variations for the individual constituent muscles in that group for all three muscle groups; for ϕ the value for the group was much lower than the mean. The mean ratios of measurements and standard deviations across the 5 subjects made in the different muscle groups has been presented graphically in

figure 8. Ratios of measurements were similar to those expected for $|G^*|$, however, were significantly different for ϕ.

4. Discussion

To the authors knowledge, the present study represents the first attempt to simulate wave propagation in multiple muscles simultaneously, and the first to utilise FEA to investigate the variability of MRE measurements in the muscles of the human leg. The elastograms created from the datasets in this study bear strong resemblance to those obtained *in vivo*, notably the artefacts associated with aliasing at the boundaries in the ϕ elastograms and the definition of individual muscles in the $|G^*|$ elastograms [1, 12]. Importantly, definition remained good at noise levels below 5%; estimations in [12] demonstrated that noise for *in vivo* MRE of the leg was in the region of 2%. The present study therefore acts as further validation of the robustness of ESP to noise at levels typically seen *in vivo*.

A previous study undertaken by this group demonstrated the dependence of MRE measurements upon the geometry of the structure under investigation [13]. This has potentially significant implications upon studies that are attempting to compare measurements from multiple individuals, since there is often a large degree of variability in the shape and size of anatomical structures. Variability of measurements was dependent upon the muscle investigate and the level of noise applied. The most reproducible measurements of individual muscles for $|G^*|$ typically came from muscles in the medial and hamstring muscle groups, whilst conversely, the least variable measurements tended to be made in the quadriceps muscles. These results were reflected in the coefficient of variation values for the overall muscle groups. In the quadriceps group, the vastus medialis obtained the highest coefficient of variation. In several of the $|G^*|$ elastograms (figure 4), there appeared to be a bright artefact within this muscle that potentially caused the higher variability seen. Further work is required to identify the source of this artefact to assess whether it is likely to be present *in vivo*. Variability of ϕ measurements was greatly reduced in the individual muscles in comparison to $|G^*|$. The presence of artefacts was much more prevalent in the elastograms (figure 4), particularly around the boundaries between muscles, and in superficial regions. Averaging ϕ values over muscle groups was a much more effective way of achieving reproducible measurements, however, the ratio of the measured values from one group to another was significantly different than expected.

This suggested that the influence of artefacts was more consistent over the larger groups than in the individual muscles.

There did not appear to be a relationship between the coefficients of variation for $|G^*|$ and ϕ, suggesting that measurements of these two properties are influenced by different factors. In this regard it should be noted that noise typically had a limited, but different influence on the coefficient of variation of $|G^*|$ and ϕ measurements (figure 6). Whilst it typically caused increased variability across the measurements of $|G^*|$, it tended to decrease the variability of measurements of ϕ. Inspection of the elastograms showed that in both cases, noise tended to increase the size and number of artefacts producing a less smooth elastogram, and resulting in poorer definition of individual muscles (figure 5). As previously discussed, the coefficient of variation for ϕ measurements was strongly influenced by the presence of artefacts, even at zero or low levels of noise, whilst for $|G^*|$ artefacts were not as prevalent, and therefore did not have as great an influence on variability. Inspection of the ϕ elastograms demonstrated that at high noise levels some muscles (such as the gracilis), were almost totally dominated by artefact. For ϕ, values can only vary from 0 to 2π, with artefacts typically represented by high values. It is therefore likely that whilst measurements were increasingly inaccurate at high noise levels, the influence of the artefact became more consistent across the set of geometries, and the variability decreased as a result.

The lack of positive correlation between expected and measured rankings for ϕ prompts caution in its mapping, implying that measured values from different muscles within the same individual are not directly comparable to one another. This point is further emphasised by the lack of agreement between the measured and expected values (figure 6 a-b), with large overestimations in several of the muscles. In contrast, the data suggests that mapping using $|G^*|$ has far greater validity. Measurements of the individual muscles were relatively accurate, whilst there was a strong positive correlation between the measured and expected rankings. In this respect, the influence of artefacts should again be noted. The highest expected $|G^*|$ value for muscles studied here was in the gracilis. In all of the elastograms, the gracilis appeared brightest (figure 5), however, its measurement was ranked second. Closer inspection of the elastograms show that in each case, there is a dark artefact around the edge of the gracilis that is expected to result from aliasing, and it is likely that this artefact reduces the measurement. Removal of such artefacts would further improve the ability to map $|G^*|$ and in all likelihood, improve the accuracy of measurements. Future work should therefore place

emphasis upon achieving this.

Since prescribed material property values were based on measurements made using MRE, this study did not intend to validate the technique in the leg. It is worth noting however, that measurements of both $|G^*|$ and ϕ in this study were very similar to measurements that have been made *in vivo* [23, 28, 1]. Furthermore, visual comparison of the elastograms produced *in silico* here with those produced in previous *in vivo* studies was very favourable. Whilst previous studies by this group utilising typically idealised and simplistic geometries have tended to produce very clean elastograms with well-defined borders between different materials in the elastograms, the elastograms produced from the simulations here, and with noise applied at the levels expected *in vivo*, look remarkably similar to those produced *in vivo* [1]. Furthermore, many of the features from *in vivo* studies are well replicated in this study, such as the artefacts that are typically seen at the edge of individual anatomical features *in vivo* in ϕ elastograms that can be seen around the individual muscles here (figure 4) [12].

A limitation of this study was in the application of material properties. There are currently a limited number of studies that have investigated material properties in the leg at the frequency range of interest, and those that have, often typically investigate at a single frequency [1, 25] or studied a limited number of muscles within the leg [22, 29]. Further work to characterise all the material properties in the human leg and match them to a material model in the same manner as undertaken by [23] would be of considerable benefit to future studies that are similar to the present one. Additionally, this study has assumed that the material properties are isotropic, whereas in reality they are highly anisotropic [30]. In future studies it will be interesting to incorporate anisotropic properties and assess its influence upon wave propagation and MRE measurements.

5. Conclusions

This study developed FEA of MRE in the human thigh in models incorporating multiple muscles and surrounding tissue. In the present study this was utilised to examine the variability of measurements in 5 human thighs through ESP. Individual muscles were well defined in the elastograms, which remained robust at the noise levels expected *in vivo*. Variability of measurements in the muscles was dramatically lower in $|G^*|$ than it was in ϕ, where artefacts appeared to have a large influence. Strong correlation between the

ranking of the magnitude of expected measurements and ranking of the magnitude of actual measurements for $|G^*|$ demonstrated that mapping allows for relatively good comparison of stiffness values from different muscles in the leg, whilst a lack of positive correlation for ϕ values prompts caution as to its use in this regard.

References

[1] E. Barnhill, P. Kennedy, S. Hammer, E. van Beek, C. Brown, N. Roberts, Statistical mapping of the effect of knee extension on thigh muscle viscoelastic properties using magnetic resonance elastography., Physiol Meas 34 (12) (2013) 1675–98. doi:10.1088/0967-3334/34/12/1675.

[2] L. Debernard, L. Robert, F. Charleux, S. F. Bensamoun, Analysis of thigh muscle stiffness from childhood to adulthood using magnetic resonance elastography (MRE) technique, Clinical Biomechanics 26 (8) (2011) 836–840. doi:10.1016/j.clinbiomech.2011.04.004.

[3] P. Lew, J. Lewis, I. Story, Inter-therapist reliability in locating latent myofascial trigger points using palpation, Manual Therapy 2 (2) (1997) 87–90. doi:10.1054/math.1997.0289.

[4] R. Muthupillai, D. Lomas, P. Rossman, J. Greenleaf, A. Manduca, R. Ehman, Magnetic resonance elastography by direct visualization of propagating acoustic strain waves., Science 269 (5232) (1995) 1854–7. doi:10.1126/science.7569924.

[5] R. Muthupillai, P. Rossman, D. Lomas, J. Greenleaf, S. Riederer, R. Ehman, Magnetic resonance imaging of transverse acoustic strain waves., Magnet Reson Med 36 (1996) 266–274. doi:10.1002/mrm.1910360214.

[6] A. Manduca, R. Muthupillai, P. Rossman, J. Greenleaf, R. Ehman, Local wavelength estimation for magnetic resonance elastography, in: Proceedings of 3rd IEEE International Conference on Image Processing, Vol. 3, IEEE, 1996, pp. 527–530. doi:10.1109/ICIP.1996.560548. URL `http://ieeexplore.ieee.org/lpdocs/epic03/wrapper.htm?arnumber=560548`

[7] A. Manduca, T. Oliphant, M. Dresner, J. Mahowald, S. Kruse, E. Amromin, J. Felmlee, J. Greenleaf, R. Ehman, Magnetic resonance elastography: non-invasive mapping of tissue elasticity., Med Image Anal 5 (4) (2001) 237–54.

[8] S. Papazoglou, S. Hirsch, J. Braun, I. Sack, Multifrequency inversion in magnetic resonance elastography., Phys Med Biol 57 (8) (2012) 2329–46. doi:10.1088/0031-9155/57/8/2329.

[9] J. Guo, S. Hirsch, A. Fehlner, S. Papazoglou, M. Scheel, J. Braun, I. Sack, Towards an elastographic atlas of brain anatomy., PloS One 8 (8) (2013) e71807. doi:10.1371/journal.pone.0071807.

[10] S. Hirsch, J. Guo, R. Reiter, S. Papazoglou, T. Kroencke, J. Braun, I. Sack, MR Elastography of the Liver and the Spleen Using a Piezoelectric Driver, Single-Shot Wave-Field Acquisition, and Multifrequency Dual Parameter Reconstruction, Magnet Reson Med 71 (1) (2014) 267–277. doi:10.1002/mrm.24674.

[11] J. Braun, J. Guo, R. Lützkendorf, J. Stadler, S. Papazoglou, S. Hirsch, I. Sack, J. Bernarding, High-resolution mechanical imaging of the human brain by three-dimensional multifrequency magnetic resonance elastography at 7T, Neuroimage 90 (2014) 308–314. doi:10.1016/j.neuroimage.2013.12.032.

[12] E. Barnhill, L. Hollis, I. Sack, J. Braun, P. Hoskins, P. Pankaj, C. Brown, E. Van Beek, N. Roberts, Nonlinear Multiscale Regularisation in MR Elastography: Towards Fine Feature Mapping, Med Imag Analdoi:10.1016/j.media.2016.05.012.

[13] L. Hollis, E. Barnhill, N. Conlisk, L. Thomas-Seale, N. Roberts, P. Pankaj, P. Hoskins, Finite Element Analysis to Compare the Accuracy of the Direct and MDEV Inversion Algorithms in MR Elastography, IAENG Int J Comput Sci 43 (2) (2016) 137–146.

[14] R. J. Maughan, J. S. Watson, J. Weir, Strength and cross-sectional area of human skeletal muscle., The Journal of physiology 338 (1983) 37–49. doi:10.1002/jmor.1051770302.

[15] Q. Chen, S. Ringleb, A. Manduca, R. Ehman, K. An, A finite element model for analyzing shear wave propagation observed in magnetic resonance elastography., J Biomech 38 (11) (2005) 2198–203. doi:10.1016/j.jbiomech.2004.09.029.

[16] A. Kolipaka, K. McGee, A. Manduca, A. Romano, K. Glaser, P. Araoz, R. Ehman, Magnetic resonance elastography: Inversions in bounded media., Magnet Reson Med 62 (6) (2009) 1533–42. doi:10.1002/mrm.22144.

[17] B. Li, C. Chui, S. Ong, T. Numano, T. Washio, K. Homma, S. Chang, S. Venkatesh, E. Kobayashi, Modeling shear modulus distribution in magnetic resonance elastography with piecewise constant level sets., Magn Reson Imaging 30 (3) (2012) 390–401. doi:10.1016/j.mri.2011.09.015.

[18] K. McGee, D. Lake, Y. Mariappan, R. Hubmayr, A. Manduca, K. Ansell, R. Ehman, Calculation of shear stiffness in noise dominated magnetic resonance elastography data based on principal frequency estimation., Physics in medicine and biology 56 (14) (2011) 4291–309. doi:10.1088/0031-9155/56/14/006.

[19] L. Thomas-Seale, L. Hollis, D. Klatt, I. Sack, N. Roberts, P. Pankaj, P. Hoskins, The simulation of magnetic resonance elastography through atherosclerosis, Journal of Biomechanics 49 (9) (2016) 1781–1788. doi:10.1016/j.jbiomech.2016.04.013.

[20] D. M. McGrath, N. Ravikumar, I. D. Wilkinson, A. F. Frangi, Z. A. Taylor, Magnetic resonance elastography of the brain: An in silico study to determine the influence of cranial anatomy, Magnet Reson Med 76 (2) (2016) 645–662. doi:10.1002/mrm.25881.

[21] L. Hollis, L. Thomas-Seale, N. Conlisk, N. Roberts, P. Pankaj, P. R. Hoskins, Investigation of Modelling Parameters for Finite Element Analysis of MR Elastography, in: Computational Biomechanics for Medicine, Springer International Publishing, Cham, 2016, pp. 75–84. doi:10.1007/978-3-319-28329-6_7.

[22] D. Klatt, S. Papazoglou, J. Braun, I. Sack, Viscoelasticity-based MR elastography of skeletal muscle., Physics in medicine and biology 55 (21) (2010) 6445–59. doi:10.1088/0031-9155/55/21/007.

[23] M. Chakouch, P. Pouletaut, F. Charleux, S. Bensamoun, Viscoelastic shear properties of in vivo thigh muscles measured by MR elastography, Journal of Magnetic Resonance Imaging 43 (6) (2015) 1423–1433. doi:10.1002/jmri.25105.

[24] D. Klatt, U. Hamhaber, P. Asbach, J. Braun, I. Sack, Noninvasive assessment of the rheological behavior of human organs using multifrequency MR elastography: a study of brain and liver viscoelasticity., Phys Med Biol 52 (24) (2007) 7281–94. doi:10.1088/0031-9155/52/24/006.

[25] M. K. Chakouch, F. Charleux, S. F. Bensamoun, Quantifying the elastic property of nine thigh muscles using magnetic resonance elastography, PLoS ONE 10 (9) (2015) 1–13. doi:10.1371/journal.pone.0138873.

[26] H. Gudbjartsson, S. Patz, The Rician Distribution of Noisy MRI Data, Magnet Reson Med 34 (6) (1995) 910–912.

[27] R. Miller, R. Mazumder, B. Cowan, M. Nash, A. Kolipaka, A. Young, Determining Anisotropic Myocardial Stiffness from Magnetic Resonance Elastography: A Simulation Study, in: Functional Imaging and Modelling of the Heart: 8th International Conference, 2015, pp. 346–354.

[28] D. Klatt, Development and Application of Multifrequency Magnetic Resonance Elastography, Ph.D. thesis (2010).

[29] S. Bensamoun, S. Ringleb, L. Littrell, Q. Chen, M. Brennan, R. Ehman, K.-n. An, Determination of thigh muscle stiffness using magnetic resonance elastography., J Magn Reson Im 23 (2) (2006) 242–7. doi:10.1002/jmri.20487.

[30] D. A. Morrow, T. L. Haut Donahue, G. M. Odegard, K. R. Kaufman, Transversely isotropic tensile material properties of skeletal muscle tissue, Journal of the Mechanical Behavior of Biomedical Materials 3 (1) (2010) 124–129. doi:10.1016/j.jmbbm.2009.03.004.

Figure 1: Left: 3-D image of the segmented muscles and bone from subject 3. Right: Labelled 2-D diagram of the material properties through the centre of the same model: 1) vastus lateralis, 2) vastus intermedius, 3) rectus femoris, 4) biceps femoris short head, 5) biceps femoris long head, 6) semitendinosus, 7) semimembranosus, 8) gracilis, 9) adductor magnus, 10) adductor longus, 11) vastus medialis, 12) sartorius, 13) surrounding tissue and 14) femoral bone.

Figure 2: The load was applied to a ring of nodes, represented in red here, on the surface of the surrounding tissue in the model.

Figure 3: Diagram of the Zener model of viscoelasticity used for materials throughout this study.

Figure 4: From top to bottom: MRI scan of the leg of each subject in the central axial plane; 2-D image of segmented model; real part of the complex z-displacement at 25 Hz; real part of the complex z-displacement at 62.5 Hz; map of $|G^*|$ from noise free dataset; and map of phi from noise free dataset.

Figure 5: Elastograms of $|G^*|$ and ϕ in subject 1 at each noise level studied.

Figure 6: All graphs are from datasets with 2% noise. a) and b) Measured and expected values for $|G^*|$ and ϕ respectively. c) and d) Measured against expected ranking of measurements for $|G^*|$ and ϕ respectively. d) and e) The coefficient of variation for measurements of $|G^*|$ and ϕ respectively across the 5 muscles against the mean size of the ROI of each muscle.

Figure 7: The influence of noise level upon the coefficient of variation for $|G^*|$ (right) and ϕ (left).

Figure 8: The ratio of measurements in the from muscles group to another for $|G^*|$ (right) and ϕ (left) at a noise level of 2%.

Table 1: Summary of the number of elements, total number of nodes over which the load was applied and the force per unit node applied in each of the models.

Table 2: The parameters of the Zener model applied for different materials within the model and the expected $|G^*|$ and ϕ values when calculated using the MDEV inversion algorithm at the frequencies applied in this study.

Table 3: The coefficient of variability for $|G^*|$ and ϕ for each muscle and each group of muscles across the 5 legs that were studied at a noise level of 2%.

	No. of Elements	Nodes in Load	Force per Node (N)
Subject 1	5,478,550	46,826	2.14×10^{-4}
Subject 2	5,561,574	47,659	2.10×10^{-4}
Subject 3	6,030,959	46,267	2.16×10^{-4}
Subject 4	6,977,826	51,331	1.95×10^{-4}
Subject 5	6,131,461	52,061	1.92×10^{-4}

	Tissue	μ_1 (Pa)	μ_2 (Pa)	η (Pa·s)	$\lvert G^* \rvert$ (Pa)	ϕ (rad)
Quadriceps	Rectus Femoris	3061	4066	3.60	3438	0.27
	Vastus Intermedius	3296	4379	3.60	3653	0.25
	Vastus Lateralis	3139	4171	3.60	3509	0.26
	Vastus Medialis	3139	4171	3.60	3509	0.26
Hamstrings	Semitendinosus	3920	3340	4.29	4433	0.23
	Semimembranosus	2920	7380	4.19	3318	0.34
	Biceps Femoris LH	3420	6900	3.96	3764	0.28
	Biceps Femoris SH	3420	6900	3.96	3764	0.28
Medial	Gracilis	5200	2920	6.65	6146	0.20
	Adductor Longus	3552	4954	4.16	3978	0.27
	Adductor Magnus	3552	4954	4.16	3978	0.27
Others	Sartorius	4002	5317	4.16	4399	0.25
	Surrounding Tissue	2433	3232	4.16	2984	0.33

	Tissue	CoV $\lvert G^* \rvert$ (%)		CoV ϕ (%)	
Quadriceps	Rectus Femoris	14.4	9.4	36.1	7.5
	Vastus Intermedius	8.9		7.1	
	Vastus Lateralis	9.5		18.5	
	Vastus Medialis	18.3		25.9	
Hamstrings	Semitendinosus	9.3	6.2	10.9	7.8
	Semimembranosus	9.0		11.0	
	Biceps Femoris LH	7.5		8.1	
	Biceps Femoris SH	5.3		17.5	
Medial	Gracilis	6.0	5.2	10.5	2.3
	Adductor Longus	9.4		27.5	
	Adductor Magnus	6.8		12.5	
Others	Sartorius	21.9		12.6